International Journal of Cardiology 293 (2019) 266–271

Contents lists available at ScienceDirect

International Journal of Cardiology

journal homepage: www.elsevier.com/locate/ijcard

Combining morphological and biomechanical factors for optimal carotid plaque progression prediction: An MRI-based follow-up study using 3D thin-layer models

Qingyu Wang [a], Dalin Tang [a,b,*], Liang Wang [a], Gador Canton [c], Zheyang Wu [b], Thomas S. Hatsukami [d], Kristen L. Billiar [e], Chun Yuan [f]

[a] School of Biological Science and Medical Engineering, Southeast University, Nanjing 210096, China
[b] Mathematical Sciences Department, Worcester Polytechnic Institute, Worcester, MA 01609, USA
[c] Department of Mechanical Engineering, University of Washington, Seattle, WA 98195, USA
[d] Division of Vascular Surgery, University of Washington, Seattle, WA 98195, USA
[e] Biomedical Engineering Department, Worcester Polytechnic Institute, Worcester, MA 01609, USA
[f] Department of Radiology, University of Washington, Seattle, WA 98195, USA

ARTICLE INFO

Article history:
Received 24 February 2019
Received in revised form 24 May 2019
Accepted 2 July 2019
Available online 4 July 2019

Keywords:
Atherosclerotic plaque
Magnetic resonance imaging (MRI)
Plaque progression
Follow-up study
Carotid artery modeling

ABSTRACT

Plaque progression prediction is of fundamental significance to cardiovascular research and disease diagnosis, prevention, and treatment. Magnetic resonance image (MRI) data of carotid atherosclerotic plaques were acquired from 20 patients with consent obtained. 3D thin-layer models were constructed to calculate plaque stress and strain. Data for ten morphological and biomechanical risk factors were extracted for analysis. Wall thickness increase (WTI), plaque burden increase (PBI) and plaque area increase (PAI) were chosen as three measures for plaque progression. Generalized linear mixed models (GLMM) with 5-fold cross-validation strategy were used to calculate prediction accuracy and identify optimal predictor. The optimal predictor for PBI was the combination of lumen area (LA), plaque area (PA), lipid percent (LP), wall thickness (WT), maximum plaque wall stress (MPWS) and maximum plaque wall strain (MPWSn) with prediction accuracy = 1.4146 (area under the receiver operating characteristic curve (AUC) value is 0.7158), while PA, plaque burden (PB), WT, LP, minimum cap thickness, MPWS and MPWSn was the best for WTI (accuracy = 1.3140, AUC = 0.6552), and a combination of PA, PB, WT, MPWS, MPWSn and average plaque wall strain (APWSn) was the best for PAI with prediction accuracy = 1.3025 (AUC = 0.6657). The combinational predictors improved prediction accuracy by 9.95%, 4.01% and 1.96% over the best single predictors for PAI, PBI and WTI (AUC values improved by 9.78%, 9.45%, and 2.14%), respectively. This suggests that combining both morphological and biomechanical risk factors could lead to better patient screening strategies.

1. Introduction

Cardiovascular diseases are the major cause of unnatural death in the world [1]. Most major cardiovascular clinical events such as heart attack and stroke are linked closely to atherosclerotic vulnerable plaque progression and rupture [2]. Clinical guidelines recommend carotid endarterectomy (CEA) for patients with 60–99% diameter asymptomatic carotid stenosis (ACS) with low perioperative risk [3–5]. However, the average annual risk of any territory stroke in these asymptomatic patients is ≤1.6% [6–9]. Up to 98% of all CEA and carotid artery stenting procedures in asymptomatic patients in the United States (US) may be unnecessary, generating needless healthcare costs of $2 billion annually [7,10]. On the other hand, in a survey of 2226 symptomatic subjects, 61% of the subjects had carotid artery stenosis <50% [11]. It is necessary that methods to predict plaque progression and rupture are developed so

Abbreviations: AUC, Area under of the ROC curve; APWSn, Average plaque wall strain; APWS, Average plaque wall stress; ECA, External carotid artery; GLMM, Generalized linear mixed models; ICA, Internal carotid artery; LP, Lipid percent; LA, Lumen area; MRI, Magnetic resonance image; MPWSn, Maximum plaque wall strain; MPWS, Maximum plaque wall stress; MinCT, Minimum cap thickness; PA, Plaque area; PAI, Plaque area increase; PB, Plaque burden; PBI, Plaque burden increase; PWSn, Plaque wall strain; PWS, Plaque wall stress; ROC curve, Receiver operating characteristic curve; WT, Wall thickness; WTI, Wall thickness increase.

* Corresponding author at: Southeast University, Nanjing, 210096, China; Mathematical Sciences Department, Worcester Polytechnic Institute, Worcester, MA 01609, USA.
E-mail addresses: dtang@wpi.edu (D. Tang), lwang6@wpi.edu (L. Wang), gcanton@uw.edu (G. Canton), zheyangwu@wpi.edu (Z. Wu), tomhat@uw.edu (T.S. Hatsukami), kbilliar@wpi.edu (K.L. Billiar), cyuan@uw.edu (C. Yuan).

https://doi.org/10.1016/j.ijcard.2019.07.005
0167-5273/

that appropriate treatment methods could be applied in time to prevent actual drastic clinical events from happening.

The progression and rupture of atherosclerotic plaques involve complex processes including biology, biochemistry, biomechanics and pathology, etc. [12–16]. Some research teams have made great effort to explore possible indicators to predict the plaque development with in vivo images. Stone GW et al. showed that nonculprit lesions associated with recurrent events were more likely than those not associated with recurrent events to be characterized by a plaque burden of 70% or greater, or a minimal luminal area of 4.0 mm^2 or less, or to be classified on the basis of radiofrequency intravascular ultrasonography as thin-cap fibroatheromas [17]. Based on in vivo magnetic resonance imaging (MRI) data, Cai et al. introduced a human carotid plaques classification system [18]. Image-based computational plaque models were introduced and used by several groups to investigate associations between biomechanical risk factors and plaque development behaviors [19–26] and to assess clinical significance [27–30]. It was reported that plaque wall stress (PWS) was associated to plaque progression [14,19,31,32]. Direct associations between flow shear stress and advanced carotid plaques were found [33]. Some groups combined biomechanical and morphological risk factors to assess plaque vulnerability for carotid and coronary arteries [28,34–38].

We hypothesized that combining morphological and biomechanical factors would lead to better prediction results of plaque progression. In this paper, MRI data of carotid atherosclerotic plaques were acquired from 20 patients with consent obtained and 3D thin-layer models were constructed to obtain 10 morphological and mechanical risk factor values for analysis. The 10 factors included wall thickness (WT), lipid percent (LP), minimum cap thickness (MinCT), plaque area (PA), plaque burden (PB), lumen area (LA), maximum plaque wall stress (MPWS), maximum plaque wall strain (MPWSn), average plaque wall stress (APWS), and average plaque wall strain (APWSn). Wall thickness increase (WTI), plaque burden increase (PBI) and plaque area increase (PAI) were chosen as three measures for plaque progression. Generalized linear mixed models (GLMM) with 5-fold cross-validation strategy were used to calculate prediction accuracy for each predictor and identify the optimal predictor. Details are given below.

2. Methods

2.1. MR images acquisition and data processing

MRI sequence data of carotid plaques from 20 patients (all male; age: 58–84, mean = 72.8) were acquired with consent obtained at the University of Washington (UW), Seattle by the Vascular Imaging Laboratory (VIL) using protocols approved by the UW Institutional Review Board. For each patient, carotid bifurcation position and plaque characteristics (lipid core, calcifications, etc.) were used to match the MRI slices at baseline time and follow-up time (marked as T1 and T2, scan time intervals: 18 months). Slice distance was kept the same at both scans. The axial distance between the non-bifurcation slice position and the bifurcation position slice was used to match the MRI slices from baseline time and follow-up time. For each slice, the geometries (mainly the centroid of their lumen) of external carotid artery (ECA) and internal carotid artery (ICA) were used to match ICA slices circumferentially at baseline and follow-up. Patient-specific cuff systolic and diastolic arm pressures were collected and used for plaque mechanical model. The procedures of data acquisition and image segmentation are detailed in our previous published articles and are omitted here [39]. Fig. 1 gave one example of matched MR images and the corresponding image segmentation contour plots at baseline and follow-up.

2.2. Computational models and solution methods

A 3D thin-layer modeling approach was used to obtain plaque stress and strain conditions. For every slice, 3D thin-layer model was made by adding a slice thickness of 0.5 mm [38]. The pre-shrink-stretch process was used on the construction of 3D thin-layer model and the component-fitting mesh generation technique were used the same as it was done in regular 3D full vessel models [33]. The hyperelastic, homogeneous, incompressible, isotropic vascular hypothesis was adopted for carotid artery [38]. The nonlinear modified Mooney-Rivlin (M-R) model was selected as the material model for carotid vessel and plaque components [40]. The strain energy function of modified M-R model was given by:

$$W = c_1(I_1-3) + c_2(I_2-3) + D_1[\exp(D_2(I_1-3))-1] \quad (1)$$

$$I_1 = \sum C_{ii}, I_2 = 0.5\left(I_1^2 - C_{ij}C_{ij}\right), i,j = 1,2,3 \quad (2)$$

where $\boldsymbol{C} = [C_{ij}] = \boldsymbol{X}^T\boldsymbol{X}$ is the right Cauchy-Green deformation tensor. I_1, is the first strain invariant and I_2 is the second strain invariants of $\boldsymbol{C}$, $\boldsymbol{X} = [X_{ij}] = [\partial x_i/\partial a_j]$, where a_j is the original location and x_i is the current location. The values of c_1, c_2, D_1, and D_2 constitute the material parameter set. M-R model was chosen because it could be consistent with the carotid vessel material properties measured by uniaxial and biaxial mechanical testing data [41]. The following material parameters were used in our models on the current literature and our own previous publications [39,41]: vessel and fibrous cap: c_1 = 36.8 kPa, D_1 = 14.4 kPa, D_2 = 2; lipid core/hemorrhage: c_1 = 2 kPa, D_1 = 2 kPa, D_2 = 1.5; loose matrix: c_1 = 18.4 kPa, D_1 = 7.2 kPa; D_2 = 1.5; calcification: c_1 = 368 kPa, D_1 = 144 kPa, D_2 = 2.0. c_2 = 0 for all materials. The patient-specific 3D thin-layer models were solved by ADINA (Adina R &D, Watertown, MA) following procedures in [40].

2.3. Morphological and biomechanical risk factors

Two hundred and one (201) matched slices from 20 patients were usable for our study. For each matched slice, 100 evenly-spaced points from the lumen were selected and values of the 10 morphological and biomechanical risk factors were obtained for statistical analysis. Each slice was divided into 4 quarters with each quarter containing 25 evenly-spaced nodal points on the lumen, each lumen nodal point was connected to a corresponding point on vessel outer-boundary using a Piecewise Equal-Step method to deal with irregular non-circular plaque morphologies (see Fig. 2) [26]. The wall thickness (WT) was defined as the distance between each nodal point on the lumen and corresponding point on the out-boundary. Cap thickness was defined as the length of the line connecting the lipid point and lumen point (use wall thickness if there is no lipid core in the slice). The minimum cap thickness (MinCT) is the minimum value of cap thickness of a slice. Fig. 2 shows the definitions of these morphological features. Lumen area (LA) is the area inside the lumen contour. Plaque area (PA) is the area bounded by the lumen contour and out-boundary. The area of a lipid core was defined as lipid area. Plaque burden (PB) and lipid percent (LP) was defined by:

$$\mathrm{PB} = \mathrm{PA}/(\mathrm{PA}+\mathrm{LA}) \quad (3)$$

$$\mathrm{LP} = \text{Lipid Area}/\mathrm{PA} \quad (4)$$

The maximum principal stress and strain were defined as plaque wall stress (PWS) and strain (PWSn) at 100 nodal points on the lumen. Maximum plaque wall stress (MPWS) was the maximum value of PWS among 100 nodal points on the lumen. Average plaque wall stress (APWS) was the mean value of PWS at 100 nodal points on the lumen. Maximum plaque wall strain (MPWSn) and average plaque wall strain (APWSn) have similar definitions to MPWS and APWS of each slice.

2.4. Measurement of plaque progression

Vessel plaque burden increase (PBI), plaque area increase (PAI) and wall thickness increase (WTI) from baseline to follow-up were three commonly used measures and defined by:

$$\mathrm{WTI} = \mathrm{WT}_{\mathrm{follow-up}} - \mathrm{WT}_{\mathrm{baseline}} \quad (5)$$

$$\mathrm{PBI} = \mathrm{PB}_{\mathrm{follow-up}} - \mathrm{PB}_{\mathrm{baseline}} \quad (6)$$

$$\mathrm{PAI} = \mathrm{PA}_{\mathrm{follow-up}} - \mathrm{PA}_{\mathrm{baseline}} \quad (7)$$

2.5. Prediction model and strategy

Generalized linear mixed models (GLMM) were used as the prediction model. The binary responses for the measures of plaque progression (PBI, PAI, or WTI) were adopted to find the best predictor(s) [37]. PBI was taken as an example to illustrate the training and testing process of our GLMM model. The same process was also applied to WTI and PAI. For a selected slice, we set PBI = 1 if PBI > 0 or PBI = 0 if PBI ≤ 0. The GLMM model is defined as [37,42]:

$$y_{ij} = E\left(y_{ij}|b_j\right) + \varepsilon_{ij} \quad (8)$$

$$\mathrm{logit}\left(E\left(y_{ij}|b_j\right)\right) = \beta_0 + \beta_1 x1_{ij} + \beta_2 x2_{ij} + \ldots + b_j \quad (9)$$

where y_{ij} is the binary response of PBI and $E(y_{ij}|b_j) = P(y_{ij} = 1|b_j)$ is the probability on the ith slice of the jth patient. $\mathrm{logit}(x) = \log(x/(1-x))$ is the binomial link function. $x1_{ij}$, $x2_{ij}$, etc. are the risk factors, which were used to predict plaque progression. β_0, β_1, etc. are the fixed-effect coefficients, b_j and ε_{ij} are the random effect terms and the random error terms of GLMM. R function glmmPQL was used to estimate the term values by fitting GLMM [43].

A 5-fold cross-validation strategy was adopted to calculate prediction accuracy for each single predictor and identify the optimal predictor [37]. All 201 MRI slices

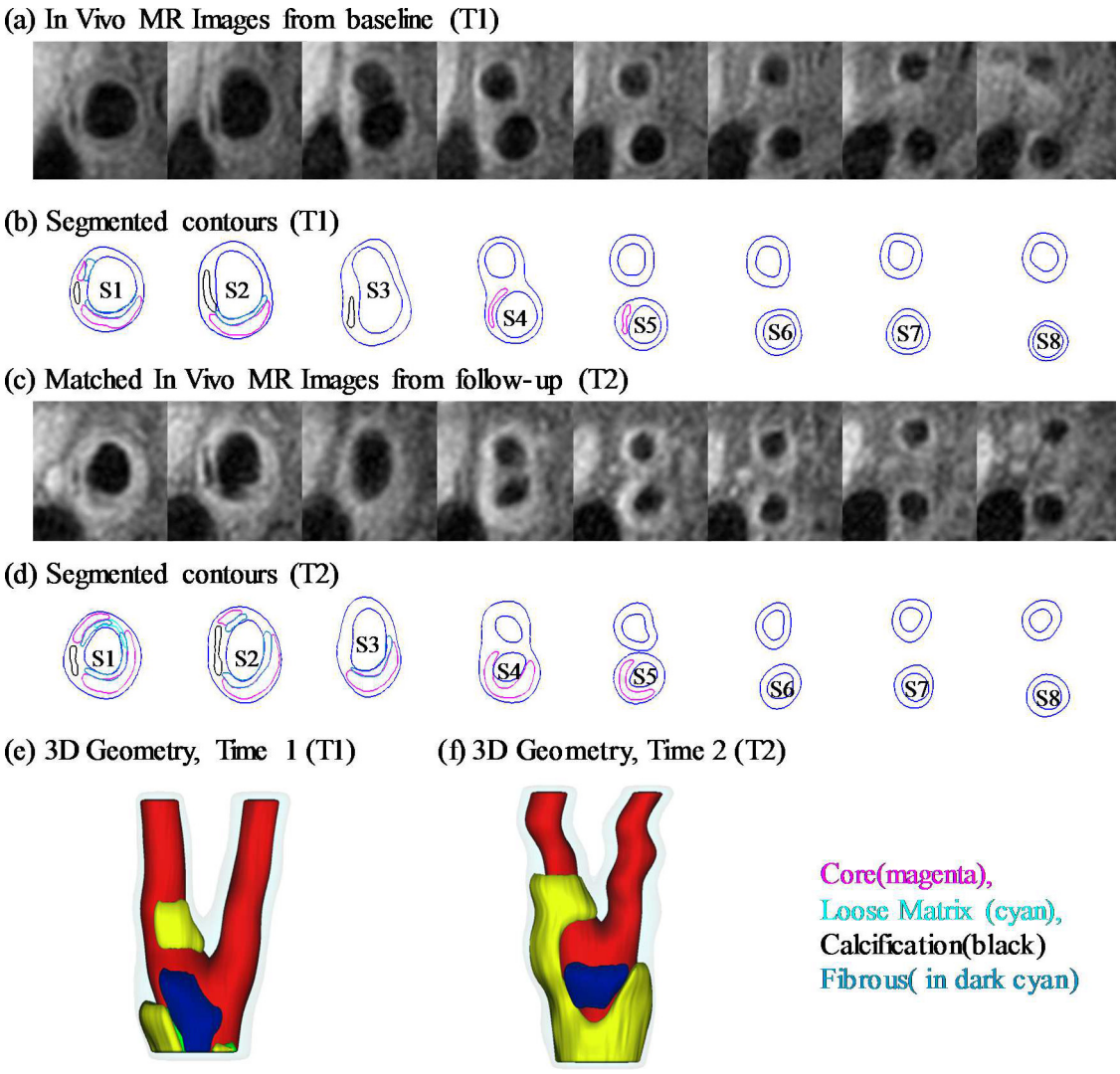

Fig. 1. Matched MR images and segmented contour plots of sliced from baseline scan and follow-up scan. (a) 8 in vivo MR images from baseline; (b) segmented contours for 8 MRI slices from baseline; (c) matched 8 in vivo MR images from follow-up; (d) segmented contours for 8 MRI slices from baseline; (e) 3D plaque geometry from baseline (Yellow: lipid; blue: calcification; light blue: outer wall; red: lumen.); (f) 3D plaque geometry from follow-up (Yellow: lipid; blue: calcification; light blue: outer wall; red: lumen).

were randomly divided into 4 training subgroups and 1 verification subgroup. The training subgroups were used for model fitting, and the verification subgroup was used to estimate the model. Sensitivity is the probability of detecting a PBI = 1 slice in the PBI = 1 class of validation subgroup. Specificity is the probability of detecting a PBI = 0 slice in the PBI = 0 class of validation subgroup. All combinations of 10 risk factors were feed to GLMM and the prediction accuracy of each predictor

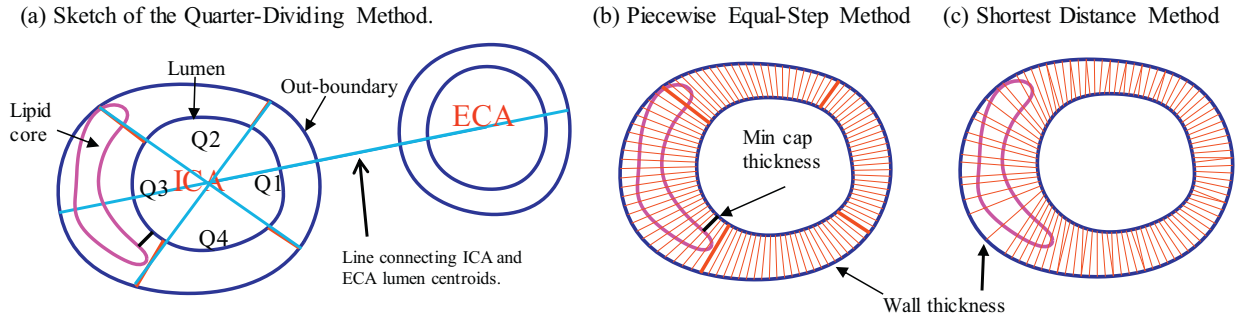

Fig. 2. Schematic drawing demonstrating the Piecewise Equal-Step method for vessel wall thickness and the quarter-dividing method. (a) Sketch of the quarter-dividing method. A line connecting the centroids of ICA and ECA lumen area was determined first. Then Q1 was determined so that the intersection of the lumen and the centerline was chosen as a data point and Q1 contains 12 data points on each side of the center line; (b) Piecewise equal-step method; (c) Shortest distance method: for every selected data point on lumen, a point on the out-boundary with the shortest distance was chosen as the matching point. This method leads to un-even representation of the out-boundary. Colour used: magenta: lipid; blue: outer wall and lumen; red: wall thickness; black: Min cap thickness.

Table 1
Prediction sensitivity and specificity, AUC value of PBI, PAI and WTI using one single risk factor and optimal predictor among all combinations.

Predictor	ProbCutoffs	Sensitivity	Specificity	Sensi + Speci	AUC
Prediction results for PBI					
LA + PA + LP + WT + MPWS + MPWSn	0.6347	0.6984	0.7162	1.4146	0.7158
LA	0.6297	0.7183	0.6419	1.3601	0.6540
APWSn	0.6243	0.6944	0.6419	1.3363	0.6342
MPWS	0.6355	0.6905	0.6419	1.3324	0.6576
PB	0.5921	0.7222	0.5685	1.2907	0.6362
LP	0.6547	0.6000	0.5850	1.1850	0.5867
MinCT	0.6987	0.502	0.6419	1.1439	0.5724
MPWSn	0.6102	0.6255	0.5170	1.1425	0.5568
WT	0.4873	0.7952	0.2500	1.0452	0.4763
APWS	0.7219	0.3400	0.6875	1.0275	0.4936
PA	0.7287	0.3855	0.6370	1.0225	0.4736
Prediction results for PAI					
PA + PB + WT + MPWS + MPWSn + APWSn	0.4570	0.7917	0.5109	1.3025	0.6657
LA	0.5811	0.4907	0.6940	1.1846	0.6064
MPWSn	0.3907	0.8920	0.2912	1.1832	0.6084
PA	0.6608	0.2710	0.8611	1.1321	0.5813
APWS	0.4730	0.7383	0.3859	1.1242	0.5628
MinCT	0.3721	0.9202	0.2099	1.1301	0.5546
MPWS	0.6505	0.3081	0.8011	1.1092	0.5420
APWSn	0.5789	0.4512	0.6538	1.1050	0.5246
WT	0.6558	0.2817	0.7845	1.0662	0.5019
PB	0.7252	0.1596	0.9000	1.0596	0.5007
LP	0.4741	0.6916	0.3497	1.0413	0.4960
Prediction results for WTI					
PA + PB + WT + LP + MinCT + MPWS + MPWS	0.6481	0.6025	0.7115	1.3140	0.6552
PA	0.5479	0.7951	0.4936	1.2887	0.6415
WT	0.5691	0.7314	0.5226	1.2540	0.6097
APWSn	0.5721	0.7107	0.5226	1.2333	0.6362
MPWS	0.6367	0.5643	0.6581	1.2224	0.6163
LA	0.6462	0.5226	0.6883	1.2109	0.6176
LP	0.4679	0.7963	0.4076	1.2039	0.6275
MinCT	0.5696	0.7190	0.4737	1.1927	0.5828
PB	0.6047	0.6132	0.5613	1.1745	0.5896
MPWS	0.6374	0.6175	0.5524	1.1700	0.5654
APWS	0.6387	0.5169	0.5197	1.0367	0.4978

was selected from the point on the ROC (receiver operating characteristic) curve with the highest sum of specificity and sensitivity. The area under the ROC curve (AUC) was used to assess the predictive power of each predictor.

3. Results

3.1. Combination of predictors for PBI improved AUC value by 9.45% over best single predictor

A total of 1023 (2^10–1) combinations of 10 risk factors at baseline were selected to determine the optimal predictor with the highest prediction accuracy. Table 1 shows the results for PBI prediction using 10 single predictors and the optimal predictor. LA was the best single predictor for PBI with the highest prediction accuracy (1.3601), and the AUC is 0.6540, followed by APWSn (1.3363) with AUC = 0.6342. The combination of LA, PA, LP, WT, MPWS, and MPWSn (marked as LA + PA + LP + WT + MPWS + MPWSn) gave the best prediction accuracy (1.4146), with AUC = 0.7158. The combinational predictor improves the AUC by 9.45%, and 4.01% in prediction accuracy compared to those given by LA, the best single predictor. The ROC curve of optimal predictor LA + PA + LP + WT + MPWS + MPWSn are given in Supplement Fig. 3.

3.2. The optimal combination of predictors for PAI prediction

Similar to the prediction process of PBI, Table 1 also summarizes the prediction results for PAI using single predictors and the optimal predictor at baseline. LA was once again the best single predictor for PAI with the highest prediction accuracy (1.1846) with AUC = 0.6064, followed by MPWSn (1.1832) with AUC = 0.6084. The combination of PA, PB, WT, MPWS, MPWSn and APWSn (marked as PA + PB + WT + MPWS + MPWSn + APWSn) gave the best prediction accuracy (1.3025), and the AUC value is 0.6657. The prediction accuracy values and AUC values for PAI were lower than those for PBI. The combinational predictor improves the AUC by 9.78%, and 9.95% in prediction accuracy compared to those given by LA, the best single predictor. The ROC curve of the optimal predictor PA + PB + WT + MPWS + MPWSn + APWSn are given in Supplement Fig. 4.

3.3. The optimal combination of predictors for WTI prediction

Table 1 shows that PA was the best single predictor for WTI with highest prediction accuracy (1.2887) with AUC = 0.6415, followed by WT (1.2540), with AUC = 0.6097. The combination of PA, PB, WT, LP, MinCT, MPWS and MPWS (marked as PA + PB + WT + LP + MinCT + MPWS + MPWS) was the best predictor with prediction accuracy as 1.3140, with AUC = 0.6552. The combination predictor still had better prediction accuracy and AUC value over those given by best single predictor. Supplement Fig. 5 shows the ROC curve using the optimal predictor PA + PB + WT + LP + MinCT + MPWS + MPWS at baseline for predicting WTI.

4. Discussion

4.1. Combining morphological and biomechanical risk factors for carotid plaque progression prediction

In the prediction of plaque progression, the combinational predictors improved prediction accuracy by 9.95%, 4.01% and 1.96% over the best single predictors for PAI, PBI and WTI, respectively. When using

Table 2
Correlation results between plaque progression (WTI) and the risk factors (PWS, PWSn, & WT) using 3D full vessel model and 3D thin-layer model at baseline (T1) and follow up (T2). ('+' means the correlation is consistent, '−' means the correlation is inconsistent).

Slices	Nodes	3D full vessel		3D thin-layer		Agreement
		r	p	r	p	
WTI vs WT						
1	100	−0.5286	0.0000	−0.5424	0.0000	+
2	100	−0.7280	0.0000	−0.7152	0.0000	+
3	100	−0.7942	0.0000	−0.7946	0.0000	+
4	100	−0.2285	0.0215	−0.2221	0.0256	+
5	100	−0.5171	0.0000	−0.6203	0.0000	+
9	100	−0.1936	0.0524	−0.1755	0.0792	+
10	100	0.6105	0.0000	0.6792	0.0000	+
WTI vs PWS						
1	100	0.8018	0.0000	0.8114	0.0000	+
2	100	0.9112	0.0000	0.8578	0.0000	+
3	100	0.4548	0.0000	0.6300	0.0000	+
4	100	−0.1664	0.0962	−0.1090	0.2777	+
5	100	0.0512	0.6113	0.2127	0.0327	+
9	100	0.3242	0.0009	−0.0871	0.3862	−
10	100	0.2895	0.0033	0.0965	0.3372	+
WTI vs PWSn						
1	100	0.7676	0.0000	0.7890	0.0000	+
2	100	0.9514	0.0000	0.8802	0.0000	+
3	100	0.3323	0.0007	0.6208	0.0000	+
4	100	−0.2303	0.0205	−0.1763	0.0779	+
5	100	0.1280	0.2020	0.2160	0.0300	+
9	100	0.4063	0.0000	−0.1779	0.0750	−
10	100	0.0807	0.4222	0.0026	0.9792	+

the single morphological or biomechanical risk factor as the predictor, PA was the best single predictor for WTI, LA was the best single predictor for PBI and PAI. The single risk factor prediction AUC values were around 50%–60% and had little clinical significance which is consistent with the current literature [11]. Combinational predictors improved prediction AUC values to near 70% (71.58%, 66.57% and 65.52% for PBI, PAI and WTI, respectively). Those represented 9.45%, 9.78%, and 2.14% improvements in AUC values over those given by the best single predictors.

4.2. PBI is more predictable measure for carotid plaque progression than WTI and PAI

PB, PA and WT are three commonly used indicators, which are often used to measure atherosclerotic plaque in human carotid and coronary artery. WTI, PBI and PAI were used to evaluate plaque progression and compare their differences. Our results show that PBI was a more predictable measure for carotid plaque progression than WTI and PAI with 10 risk factors as predictive indicators. And the combinations of LA, PA, LP, WT, MPWS and MPWSn was the best predictor with prediction accuracy 1.4146 and AUC value 0.7158. The values of sensitivity and specificity were 0.6984 and 0.7162, indicating that the predictor can better predict PB changes. No matter how the plaque size changed, at least 71% of the slices could get the correct consistency between the prediction of the plaque size change and the actual plaque size change. For the other two plaque progression measurements, the optimal prediction accuracy of WTI and PAI can only reach 1.314 and 1.3025.This suggest that we may want to use PBI to measure plaque progression in future studies.

4.3. 3D thin-layer model are consistent with the 3D full vessel model correlation results

3D full vessel computational models are certainly desirable for plaque stress and strain calculations. However, 3D full vessel model construction is time consuming. 3D thin-layer modeling method was used in this paper as an approximation to full 3D models since the thin-layer model requires much less computational cost and human labor than 3D full vessel models. 3D axial stretch was still included in 3D thin-layer models, which is similar to the procedures of 3D full vessel model. That made 3D thin-layer model much better approximation to 3D full vessel model than the simple 2D models. Correlation results given in Table 2 show that results from 3D thin-layer models were consistent with those from 3D full vessel models. The agreement rate was as high as 90.48% (19 from 21, detailed in Table 2). Therefore, considering the modeling time (1 or 2 weeks) cost of 3D full vessel model, 3D thin-layer models may be used to replace 3D full vessel models to perform mechanical analysis for possible clinical implementation.

4.4. Limitations

MR has a limited imaging resolution, and the thin plaque cap cannot be detected. In this study, patient-specific vessel and plaque component material properties data were lacking and unavailable. The parameter values in the material models were selected from our previous literature [24]. Acquisition of intravascular pressure data with a noninvasive manner is still a challenge. Furthermore, larger patient size studies are necessary to further improve and validate our results. Lastly, due to potential collinearity among the predictors, generalizing the prediction accuracies to a broader population requires the assumption that the collinearity patterns remain unchanged. This assumption is to be further studied upon more data are available.

5. Conclusion

In this study, 10 morphological and biomechanical risk factors at baseline were used to predict plaque progression. The prediction results of plaque progression supported our hypothesis that the predictor combining morphology and biomechanics risk factors was more accurate than any single risk factor. 3D thin-layer models showed good agreement with 3D full vessel models.

Acknowledgement and funding

This research was supported in part by NSF grant DMS-0540684 and NIH grants R01 EB004759, R01 HL61851, P01 HL072262. Wang QY's research was supported in part by Postgraduate Research & Practice Innovation Program of Jiangsu Province grant KYCX18_0156. Tang's research was also supported in part by National Natural Science Foundation of China grant 11672001 and a Jiangsu Province Science and Technology Agency grant BE2016785.

Conflict of interest

None.

Appendix A. Supplementary data

Supplementary data to this article can be found online at https://doi.org/10.1016/j.ijcard.2019.07.005.

References

[1] World Health Organization, Global Atlas on Cardiovascular Disease Prevention and Control, World Health Organization, Geneva, 2011.
[2] M. Naghavi, P. Libby, E. Falk, et al., From vulnerable plaque to vulnerable patient: a call for new definitions and risk assessment strategies: part I, Circulation 108 (2003) 1664–1672.
[3] T.G. Brott, J.L. Halperin, S. Abbara, et al., ASA/ACCF/AHA/AANN/AANS/ACR/ASNR/CNS/SAIP/SCAI/SIR/SNIS/SVM/SVS guideline on the management of patients with extracranial carotid and vertebral artery disease, Stroke 42 (2011) e464–e540.
[4] K.I. Paraskevas, J.D. Spence, F.J. Veith, A.N. Nicolaides, Identifying which patients with asymptomatic carotid stenosis could benefit from intervention, Stroke 45 (2014) 3720–3724.
[5] J.J. Ricotta, A. Aburahma, E. Ascher, M. Eskandari, P. Faries, B.K. Lal, Updated Society for Vascular Surgery guidelines for management of extracranial carotid disease: executive summary, J. Vasc. Surg. 54 (2011) 832–836.
[6] A.R. Naylor, Time to rethink management strategies in asymptomatic carotid artery disease, Nat. Rev. Cardiol. 9 (2012) 116–124.
[7] A.R. Naylor, P.A. Gaines, P.M. Rothwell, Who benefits most from intervention for asymptomatic carotid stenosis: patients or professionals? Eur. J. Vasc. Endovasc. Surg. 37 (2009) 625–632.
[8] A.N. Nicolaides, S.K. Kakkos, E. Kyriacou, et al., Asymptomatic internal carotid artery stenosis and cerebrovascular risk stratification, J. Vasc. Surg. 52 (2010) 1486–1496. e5.
[9] J.D. Spence, D. Pelz, F.J. Veith, Asymptomatic carotid stenosis: identifying patients at high enough risk to warrant endarterectomy or stenting, Stroke 45 (2014) 655–657.
[10] A.R. Naylor, Why is the management of asymptomatic carotid disease so controversial? Surgeon 13 (2015) 34–43.
[11] H.J. Barnett, D.W. Taylor, M. Eliasziw, et al., Benefit of carotid endarterectomy in patients with symptomatic moderate or severe stenosis. North American Symptomatic Carotid Endarterectomy Trial Collaborators, N. Engl. J. Med. 339 (1998) 1415–1425.
[12] H.C. Stary, A.B. Chandler, M.D. Dinsmore, et al., A definitions of advanced types of atherosclerotic lesions and the histological classification of atherosclerosis. A report from the Committee on Vascular Lesions of the Council on Arteriosclerosis, AHA Circulation 92 (1995) 1355–1374.
[13] D.N. Ku, D.P. Giddens, C.K. Zarins, S. Glagov, Pulsatile flow and atherosclerosis in the human carotid bifurcation: positive correlation between plaque location and low and oscillating shear stress, Arteriosclerosis 5 (1985) 293–302.
[14] D. Tang, Z. Teng, G. Canton, et al., Local critical stress correlates better than global maximum stress with plaque morphological features linked to atherosclerotic plaque vulnerability: an in vivo multi-patient study, Biomed. Eng. Online 8 (2009) 15.
[15] C. Yuan, L.M. Mitsumori, K.W. Beach, K.R. Maravilla, Special review: carotid atherosclerotic plaque: noninvasive MR characterization and identification of vulnerable lesions, Radiology 221 (2001) 285–299.
[16] C. Yuan, S.X. Zhang, N.L. Polissar, et al., Identification of fibrous cap rupture with MRI is highly associated with recent transient ischemic attack or stroke, Circulation 105 (2002) 181–185.

[17] G.W. Stone, A. Maehara, A.J. Lansky, et al., A prospective natural-history study of coronary atherosclerosis, N. Engl. J. Med. 364 (2011) 226–235.
[18] J.M. Cai, T.S. Hatsukami, M.S. Ferguson, R. Small, N.L. Polissar, C. Yuan, Classification of human carotid atherosclerotic lesions with in vivo multicontrast magnetic resonance imaging, Circulation 106 (2002) 1368–1373.
[19] D. Bluestein, Y. Alemu, I. Avrahami, et al., Influence of microcalcifications on vulnerable plaque mechanics using FSI modeling, J. Biomech. 41 (2008) 1111–1118.
[20] G.C. Cheng, H.M. Loree, R.D. Kamm, M.C. Fishbein, R.T. Lee, Distribution of circumferential stress in ruptured and stable atherosclerotic lesions, a structural analysis with histopathological correlation, Circulation 87 (1993) 1179–1187.
[21] G.A. Holzapfel, M. Stadler, C.A. Schulze-Bause, A layer-specific three dimensional model for the simulation of balloon angioplasty using magnetic resonance imaging and mechanical testing, Ann. Biomed. Eng. 30 (2002) 753–767.
[22] J.R. Leach, V.L. Rayz, B. Soares, M. Wintermark, M.R. Mofrad, D. Saloner, Carotid atheroma rupture observed in vivo and FSI-predicted stress distribution based on pre-rupture imaging, Ann. Biomed. Eng. 38 (2010) 2748–2765.
[23] U. Sadat, Z. Teng, V.E. Young, et al., Impact of plaque haemorrhage and its age on structural stresses in atherosclerotic plaques of patients with carotid artery disease: an MR imaging-based finite element simulation study, Int J Cardiovasc Imaging 27 (2011) 397–402.
[24] D. Tang, C. Yang, J. Zheng, et al., 3D MRI-based multi-component FSI models for atherosclerotic plaques: a 3-D FSI model, Ann. Biomed. Eng. 32 (2004) 947–960.
[25] C. Yang, D. Tang, C. Yuan, et al., Meshless generalized finite difference method and human carotid atherosclerotic plaque progression simulation using multi-year MRI patient-tracking data, Comput. Model. Eng. Sci. 28 (2008) 95–107.
[26] C. Yang, G. Canton, C. Yuan, M. Ferguson, T.S. Hatsukami, D. Tang, Advanced human carotid plaque progression correlates positively with flow shear stress using follow-up scan data: an in vivo MRI multi-patient 3D FSI study, J. Biomech. 43 (2010) 2530–2538.
[27] H. Gao, Q. Long, S. Kumar Das, et al., Study of carotid arterial plaque stress for symptomatic and asymptomatic patients, J. Biomech. 44 (2011) 2551–2557.
[28] F.J. Gijsen, H.A. Nieuwstadt, J.J. Wentzel, H.J. Verhagen, A. van der Lugt, A.F. van der Steen, Carotid plaque morphological classification compared with biomechanical cap stress: implications for a magnetic resonance imaging-based assessment, Stroke 46 (2015) 2124–2128.
[29] Z.Y. Li, S.P. Howarth, T. Tang, et al., Structural analysis and magnetic resonance imaging predict plaque vulnerability: a study comparing symptomatic and asymptomatic individuals, J. Vasc. Surg. 45 (2007) 768–775.
[30] C. Zhu, Z. Teng, U. Sadat, et al., Normalized wall index specific and MRI-based stress analysis of atherosclerotic carotid plaques: a study comparing acutely symptomatic and asymptomatic patients, Circ. J. 74 (2010) 2360–2364.
[31] Z. Teng, G. Canton, C. Yuan, et al., 3D critical plaque wall stress is a better predictor of carotid plaque rupture sites than flow shear stress: an in vivo MRI-based 3D FSI study, J. Biomech. Eng. 132 (2010), 031007.
[32] X. Huang, C. Yang, G. Canton, M. Ferguson, C. Yuan, D. Tang, Quantifying effect of intraplaque hemorrhage on critical plaque wall stress in human atherosclerotic plaques using three-dimensional fluid-structure interaction models, J. Biomech. Eng. 134 (2012), 121004.
[33] D. Tang, R.D. Kamm, C. Yang, et al., Image-based modeling for better understanding and assessment of atherosclerotic plaque progression and vulnerability: data, modeling, validation, uncertainty and predictions, J. Biomech. 47 (2014) 834–846.
[34] H.M. Loree, R.D. Kamm, R.G. Stringfellow, R.T. Lee, Effects of fibrous cap thickness on peak circumferential stress in model atherosclerotic vessels, Circ. Res. 71 (1992) 850–858.
[35] J. Ohayon, G. Finet, A.M. Gharib, D.A. Herzka, P. Tracqui, Necrotic core thickness and positive arterial remodeling index: emergent biomechanical factors for evaluating the risk of plaque rupture, Am. J. Physiol. Heart Circ. Physiol. 295 (2008) H717–H727.
[36] D. Tang, C. Yang, J. Zheng, et al., Local maximal stress hypothesis and computational plaque vulnerability index for atherosclerotic plaque assessment, Ann. Biomed. Eng. 33 (2005) 1789–1801.
[37] L. Wang, D. Tang, A. Maehara, et al., Fluid-structure interaction models based on patient-specific IVUS at baseline and follow-up for prediction of coronary plaque progression by morphological and biomechanical factors: a preliminary study, J. Biomech. 68 (2018) 43–50.
[38] Q. Wang, D. Tang, G. Canton, et al., Impact of patient-specific in vivo vessel material properties on carotid atherosclerotic plaque stress/strain calculations, International Journal of Computational Methods (2018), 1842002.
[39] D. Tang, Z. Teng, G. Canton, et al., Sites of rupture in human atherosclerotic carotid plaques are associated with high structural stresses: an in vivo MRI-based 3D fluid-structure interaction study, Stroke 40 (2009) 3258–3263.
[40] K.J. Bathe, Theory and Modeling Guide, Vol I & II: ADINA and ADINA-F, ADINA R & D, Inc., Watertown, MA, 2002.
[41] M.H. Kural, M. Cai, D. Tang, T. Gwyther, J. Zheng, K.L. Billiar, Planar biaxial characterization of diseased human coronary and carotid arteries for computational modeling, J. Biomech. 45 (2012) 790–798.
[42] Z. Wu, C. Yang, D. Tang, In vivo serial MRI-based models and statistical methods to quantify sensitivity and specificity of mechanical predictors for carotid plaque rupture: location and beyond, J. Biomech. Eng. 133 (2011), 064503.
[43] W.N. Venables, B.D. Ripley, Modern Applied Statistics with S, Springer, New York, 2002 183–210.